



Available online at www.sciencedirect.com

ScienceDirect

Comput. Methods Appl. Mech. Engrg. 391 (2022) 114526

Computer methods in applied mechanics and engineering

www.elsevier.com/locate/cma

A novel method to impose boundary conditions for higher-order partial differential equations

Tianyi Hu, Yu Leng, Hector Gomez*

School of Mechanical Engineering, Purdue University, 585 Purdue Mall, West Lafayette, IN 47907, USA

Received 27 July 2021; received in revised form 21 October 2021; accepted 21 December 2021

Available online 15 January 2022

Abstract

Partial differential equations (PDEs) with spatial derivatives of order higher than two are receiving increasing attention, partially due to the current popularity of the phase-field method. In the finite element community, the growth of Isogeometric Analysis and other discretization schemes that employ approximation spaces with high-order continuity has fostered the use of variational formulations that avoid the use of auxiliary unknowns representing derivatives of the solution. However, one of the caveats of this approach is the accurate and efficient imposition of boundary conditions, especially on complex geometries. This paper proposes a new method to impose boundary conditions naturally in the weak form of higher-order PDEs. Our method is based on a specially-designed weak form in which the boundary conditions to be imposed are weighted by derivatives of the weight functions. This requires multiple integrations by parts which are allowed due to the smoothness of the basis functions. The Cahn–Hilliard equation and the isothermal Navier–Stokes–Norteweg equations are used as examples to demonstrate the proposed method. We show that if the solutions of the PDEs are smooth enough, the proposed variational equations and the original PDEs are equivalent. We discretize the variational equations using Isogeometric Analysis. Convergence results of the proposed method agree with the best approximation errors of the basis functions. Numerical examples illustrate the applicability of the approach to mapped geometries with non-conformal grids.

© 2021 Elsevier B.V. All rights reserved.

Keywords: Higher-order PDEs; Contact angle boundary condition; Phase-field; Cahn-Hilliard; Navier-Stokes-Korteweg

1. Introduction

Partial differential equations (PDEs) with spatial differential operators of order higher than two are receiving increasing attention in the computational mechanics community. Higher-order PDEs have traditionally been used for plate and shell analysis [1], strain-gradient elasticity [2,3], higher-order continuum descriptions of fluid flow like the Burnett equations [4,5], reduced-dimensionality flow models like the thin-film equations [6], plasma physics [7,8], and stream-function formulations of the Stokes problem [9,10].

More recently, higher-order PDEs have received renewed attention due to the emergence of phase-field theory — a modeling paradigm for problems that involve moving interfaces [11–13]. In many cases, the phase-field approach allows to reformulate a moving boundary problem for second-order PDEs as a problem on a fixed domain for a

E-mail address: hectorgomez@purdue.edu (H. Gomez).

^{*} Corresponding author.

higher-order PDE. For example, the flow of two immiscible fluids with surface tension can be represented as a moving boundary problem in which we solve the flow equations on two time-dependent domains coupled through boundary conditions at the interface (note that the interface motion is also an unknown here) or by the so-called Navier–Stokes–Cahn–Hilliard (NSCH) equations, which are a system of PDEs that needs to be solved on a *fixed* domain. When the two fluids have constant density, the unknowns in the NSCH equations are the velocity, the pressure and a phase-field which is related to the composition and identifies the location of the two fluids. Under equilibrium conditions, the phase field transitions smoothly between two constant values. The smooth (but steep) transition occurs at the interface between the two fluids, which becomes diffuse with controllable thickness. The theory of Γ -convergence [14] can be used to show that the NSCH equations converge to the classical moving boundary problem when the thickness of the interface approaches zero.

From a computational perspective, the use of the phase-field method significantly simplifies the treatment of interface problems because all computations can be performed on a fixed mesh. In addition, the singularities that occur in the moving boundary approach when the interface changes topology are not present in the phase-field formulation. For example, in the context of fluid flow, the merging or breakup of droplets can be studied without any complication arising from singularities. These advantages have made the phase-field approach increasingly popular in a number of applications, including multiphase flows [15], multicomponent flows [16], crack propagation [17], bio-membranes [18], surface PDEs [19], fluid–structure interaction [20], fluid–solid phase transitions [21], and others [22].

While the use of higher-order PDEs may dramatically simplify the computational analysis of an interface problem by allowing us to perform the computations on a fixed mesh, the discretization of higher-order operators is more difficult than the discretization of second-order operators, especially on complex geometries. In fact, the most widely used approach in the finite element community for higher-order PDEs is the reformulation of the PDE as a system of lower-order PDEs [23-29]. For example, the bi-harmonic equation can be split into two Poisson equations, which can be discretized using standard finite element methods — this is usually referred to as the split method. The direct discretization of the bi-harmonic equation (usually referred to as direct method) requires the use of basis functions that are at least C^1 -continuous across the element boundaries, which is extremely difficult with traditional finite elements on complicated three-dimensional geometries. The appearance of Isogeometric Analysis (IGA) [30], however, has opened new opportunities to discretize higher-order equations through the direct method [31] due to the higher-order continuity of splines across the element boundaries even on mapped geometries. IGA, thus, facilitates the use of the direct method which is in principle preferable because it does not introduce additional unknowns that increase the size of the algebraic problem. Perhaps even more importantly, in some cases, the split method cannot be used. For example, in the field of plate analysis, it is known that the original bi-harmonic equation for a simply supported Kirchhoff plate on a non-convex polygonal domain is not equivalent to the second-order system of two Poisson equations [32].

Although the appearance of IGA has reinvigorated the use of the direct method, the imposition of boundary conditions remains problematic in some cases. From a conceptual point of view, the most straightforward approach to impose boundary conditions for a higher-order PDE in the direct method requires enforcing non-trivial constraints on the finite element spaces [33,34]. For example, we may need to impose constraints on the degrees of freedom of the solution to strongly enforce the value of the derivative of the solution in the direction normal to the boundary, which can be very difficult to do on complicated geometries with non-conformal mappings. Therefore, some alternatives to this approach have been proposed, including the penalty method [35,36], Nitsche's method [37] or the method of Lagrange multipliers [38]. However, none of these methods are completely satisfactory. The use of Lagrange multipliers increases the size of the algebraic system and induces a saddle-point structure in the problem which precludes an arbitrary choice of the interpolation of the main unknown and the Lagrange multipliers. The penalty method is not consistent, results in sub-optimal convergence rates even with a judicious choice of the penalty parameter and leads to ill-conditioned algebraic problems. Nitsche's method is an improvement of the penalty method that restores consistency to the variational formulation and optimal convergence rate, but still requires adjusting a parameter and may lead to ill-conditioned problems. The imposition of boundary conditions is currently a significant limitation of the direct method, and indeed, some publications resorted to the split method just because it is easier to impose boundary conditions when we split the higher-order PDE into a system of lower-order equations. For example, contact angle boundary conditions in multiphase or multicomponent flows appear naturally in the weak form of the split method [39,40].

Here, we propose a new algorithm to impose general boundary conditions in the direct method. The proposed algorithm can be used on non-conformal grids and mapped geometries. We illustrate the approach using relevant problems of multiphase and multicomponent flows, imposing dynamic and static, non-trivial contact angle boundary conditions. The Cahn–Hilliard equation and the isothermal Navier–Stokes–Korteweg equations are used for illustration. We show that if the solutions are smooth enough, the proposed variational equations and the PDEs are equivalent. IGA is adopted to discretize the variational equations. We present several numerical examples that indicate that the proposed method achieves optimal rates of convergence. We believe this work offers a general, simple and efficient solution to the imposition of boundary conditions in the direct discretization of higher-order PDEs.

2. Problem formulation

In this section, we introduce two examples of higher-order PDEs, namely, the Cahn-Hilliard equation and the isothermal Navier-Stokes-Korteweg equations. We use the following notation for the rest of the paper. The spatial dimension is denoted as d. Let $\Omega \subset \mathbb{R}^d$ be an open, bounded domain with Lipschitz boundary, which is denoted as $\Gamma := \partial \Omega$. The vector \mathbf{n} represents the unit outward normal to Γ . A finite time interval of interest is denoted as $\mathbb{I}_T = (0, T)$, for T > 0.

2.1. The Cahn-Hilliard equation

The Cahn-Hilliard equation is a fourth-order PDE, which is widely used to describe phase separation of two immiscible fluids [41,42].

2.1.1. Strong form

We define $c(x, t) : \Omega \times \mathbb{I}_T \mapsto \mathbb{R}$ as the difference between the mass fraction of the two components in a binary mixture. In what follows, we will simply refer to c as concentration or phase field for simplicity. We consider the following initial and boundary value problem associated with the Cahn–Hilliard equation:

$$\frac{\partial c}{\partial t} = M\Delta \left(f'(c) - \epsilon^2 \Delta c \right), \text{ in } \Omega \times \mathbb{I}_T, \tag{1a}$$

$$\nabla \left(f'(c) - \epsilon^2 \Delta c \right) \cdot \mathbf{n} = 0, \text{ on } \Gamma \times \mathbb{I}_T, \tag{1b}$$

$$\nabla c \cdot \mathbf{n} = g(c), \text{ on } \Gamma \times \mathbb{I}_T,$$
 (1c)

$$c(\mathbf{x},0) = c_0(\mathbf{x}), \text{ in } \Omega \times \{0\}, \tag{1d}$$

where M > 0 is the mobility, which we assumed constant; $\epsilon > 0$ represents the length scale of the diffuse interface; f'(c) is the first derivative of a double potential, f(c); c_0 is the initial concentration; and Eq. (1c) represents a dynamic contact angle boundary condition [43–45], i.e.,

$$g(c) = -\frac{1}{\epsilon^2} f'_w(c) - D_w \frac{\partial c}{\partial t},\tag{2}$$

where $f_w(c)$ is proportional to the specific wall energy, and D_w is a constant obtained from experiments or molecular kinetic theory. If $D_w = 0$, Eq. (2) reduces to the form of the static contact angle boundary condition, namely, $\nabla c \cdot \mathbf{n} = -f'_w(c)/\epsilon^2$.

2.1.2. Dimensionless form

All physical quantities in the Cahn-Hilliard equation can be described using fundamental units in the time and length measurement class. The scaling constants that we choose here (scaling the units of length and time by L_0 and $T_0 = L_0^2/M$, respectively) are slightly different from those used in [31]. We will use an overhat to denote non-dimensionalized quantities. After scaling, Eq. (1) becomes

$$\frac{\partial c}{\partial \hat{t}} = \hat{\Delta} \left(f'(c) - \hat{\epsilon}^2 \hat{\Delta} c \right), \text{ in } \hat{\Omega} \times \mathbb{I}_{\hat{T}}, \tag{3a}$$

$$\hat{\nabla} \left(f'(c) - \hat{\epsilon}^2 \hat{\Delta} c \right) \cdot \mathbf{n} = 0, \text{ in } \hat{\Gamma} \times \mathbb{I}_{\hat{T}}, \tag{3b}$$

$$\hat{\nabla}c \cdot \mathbf{n} = \hat{g}(c), \text{ in } \hat{\Gamma} \times \mathbb{I}_{\hat{\tau}}, \tag{3c}$$

$$c(\hat{\mathbf{x}},0) = c_0(\hat{\mathbf{x}}), \text{ in } \hat{\Omega} \times \{0\}, \tag{3d}$$

where $\hat{\epsilon} = \epsilon/L_0$ and $\hat{D}_w = D_w M/L_0$ are the dimensionless groups that determine the solution. Note that we did not use the overhat for quantities that were already dimensionless before scaling. The dimensionless form of Eq. (2) is

$$\hat{g}(c) = -\frac{1}{\hat{\epsilon}^2} \hat{f}'_w(c) - \hat{D}_w \frac{\partial c}{\partial \hat{t}}, \text{ with } \hat{f}_w(c) = \frac{\hat{\epsilon} \left(c^3 - 3c\right)}{3\sqrt{2}} \cos \theta, \tag{4}$$

where θ is the equilibrium contact angle between the mixture interface and the boundary [46]. The double well potential is given by

$$f(c) = \frac{1}{4} \left(1 - c^2 \right)^2. \tag{5}$$

2.2. The isothermal Navier-Stokes-Korteweg equations

The second example of higher-order PDE is given by the Navier–Stokes–Korteweg equations, which are a system of third-order PDEs used to model the flow of a two-phase single-component system that undergoes liquid-vapor transformations [47], such as, boiling [48] and cavitation [49].

We can scale the original model equations using fundamental units of mass, length, time and temperature. We use the dimensionless form of the equations presented in [50]. Denoting the density of the fluid as $\hat{\rho}: \hat{\Omega} \times \mathbb{I}_{\hat{T}} \mapsto \mathbb{R}^+$ and the velocity field as $\hat{u}: \hat{\Omega} \times \mathbb{I}_{\hat{T}} \mapsto \mathbb{R}^d$, we write the dimensionless form of the Navier–Stokes–Korteweg equations as

$$\frac{\partial \hat{\rho}}{\partial \hat{t}} + \hat{\nabla} \cdot (\hat{\rho} \hat{\boldsymbol{u}}) = 0, \text{ in } \hat{\Omega} \times \mathbb{I}_{\hat{T}}, \tag{6a}$$

$$\frac{\partial \left(\hat{\rho}\hat{\boldsymbol{u}}\right)}{\partial \hat{t}} + \hat{\nabla} \cdot \left(\hat{\rho}\hat{\boldsymbol{u}} \otimes \hat{\boldsymbol{u}} + \hat{p}\boldsymbol{I}\right) - \frac{1}{R_e}\hat{\nabla} \cdot \hat{\boldsymbol{\tau}} - W_e^2 \hat{\nabla} \cdot \hat{\boldsymbol{\zeta}} = \hat{\boldsymbol{f}}\hat{\rho}, \text{ in } \hat{\Omega} \times \mathbb{I}_{\hat{T}}, \tag{6b}$$

$$\hat{\boldsymbol{u}} = \boldsymbol{0}, \text{ in } \hat{\boldsymbol{\Gamma}} \times \mathbb{I}_{\hat{\boldsymbol{\tau}}},$$
 (6c)

$$\hat{\nabla}\hat{\rho}\cdot\boldsymbol{n}=\hat{s}(\hat{\rho}), \text{ in } \hat{\Gamma}\times\mathbb{I}_{\hat{\tau}},\tag{6d}$$

$$\hat{\rho}(\hat{\mathbf{x}}, 0) = \hat{\rho}_0(\hat{\mathbf{x}}), \text{ in } \hat{\Omega} \times \{0\}, \tag{6e}$$

$$\hat{\boldsymbol{u}}(\hat{\boldsymbol{x}},0) = \hat{\boldsymbol{u}}_0(\hat{\boldsymbol{x}}), \text{ in } \hat{\Omega} \times \{0\}, \tag{6f}$$

where \hat{p} is the thermodynamic pressure, I is the d × d identity tensor, R_e and W_e are the Reynolds number and the Weber number respectively, $\hat{\tau}$ represents the viscous stress tensor, $\hat{\zeta}$ is the Korteweg stress tensor, \hat{f} denotes the body force per unit mass and is neglected for the rest of the work, Eq. (6d) is the contact angle boundary condition, and $\hat{\rho}_0$ and \hat{u}_0 are the initial data for the fluid density and velocity respectively.

The expression of the thermodynamic pressure \hat{p} depends on the choice of equation of state. We consider the van der Waals equation, which is widely used for liquid-vapor phase transformations,

$$\hat{p} = \frac{8}{27} \frac{\hat{\Theta}\hat{\rho}}{1 - \hat{\rho}} - \hat{\rho}^2,\tag{7}$$

where $\hat{\theta}$ represents the dimensionless absolute temperature. Assuming the Stokes hypothesis [50] is satisfied, we have the viscous stress tensor as

$$\hat{\boldsymbol{\tau}} = \left(\hat{\nabla}\hat{\boldsymbol{u}} + \hat{\nabla}^T\hat{\boldsymbol{u}}\right) - \frac{2}{3}(\hat{\nabla}\cdot\hat{\boldsymbol{u}})\boldsymbol{I}.$$
 (8)

The Korteweg stress tensor is defined by

$$\hat{\boldsymbol{\zeta}} = \left(\hat{\rho}\hat{\Delta}\hat{\rho} + \frac{1}{2}|\hat{\nabla}\hat{\rho}|^2\right)\boldsymbol{I} - \hat{\nabla}\hat{\rho}\otimes\hat{\nabla}\hat{\rho}.\tag{9}$$

We adopt the following dimensionless static contact angle boundary condition, given in [47],

$$\hat{s}(\hat{\rho}) = -|\hat{\nabla}\hat{\rho}|\cos\theta. \tag{10}$$

In what follows we will use the dimensionless form of the Cahn–Hilliard Eq. (3) and the isothermal Navier–Stokes–Korteweg Eqs. (6). To simplify the notation, we omit the overhat henceforth. We remark that the major contribution of this work is proposing a novel method to impose the nontrivial dynamic and static contact angle boundary conditions, i.e., Eqs. (4), (4) and (3c) for the Cahn–Hilliard equation, and Eqs. (10) and (6d) for the Navier–Stokes–Korteweg equations.

3. Variational formulations

In this section, we propose novel variational formulations of the two example model equations introduced in the previous section, the Cahn–Hilliard equation and the isothermal Navier–Stokes–Korteweg equations. Compared to the traditional direct method, the proposed variational formulations involve one more step of integration by parts. This permits the natural implementation of realistic contact angle boundary conditions. For comparison purposes, we also present more traditional variational formulations based on the idea of splitting a high-order PDE into multiple lower-order PDEs. We refer to this approach as split method.

We start by introducing more notations that are used for the remainder of the paper. Let $U \in \mathcal{U}$ be the solution or trial function to the PDEs of our interest and the corresponding test function is $V \in \mathcal{V}$, for some functional spaces \mathcal{U} and \mathcal{V} . The functions U and V are subject to change for different PDEs and variational formulations, and thus may contain one or multiple components. We further assume $U(t) \in C(\mathbb{I}_T)$. Thus we drop the dependence on t and only work in the spatial functional spaces. We denote (\cdot, \cdot) the standard L^2 inner product over Ω , and use $\langle \cdot, \cdot \rangle$ to represent the duality pairing over Γ .

3.1. Variational formulations of the Cahn-Hilliard equation

We introduce the variational formulations of the Cahn-Hilliard equation using the proposed and the split methods.

3.1.1. Proposed method

In this subsection, we let $U = \{c\} \in \mathcal{U}$ and $V = \{v\} \in \mathcal{V}$, for $\mathcal{U} = H^4(\Omega)$ and $\mathcal{V} = H^3(\Omega)$. Because there is only one unknown, c, for the proposed method, we can use c and U, or v and V interchangeably. Suppose $U \in \mathcal{U}$ satisfies Eq. (3), then $\forall V \in \mathcal{V}$,

$$0 = \left(\frac{\partial c}{\partial t} - \Delta \left(f'(c) - \epsilon^2 \Delta c \right), v \right)$$

$$= \left(\frac{\partial c}{\partial t}, v\right) + \left(\nabla f'(c), \nabla v\right) - \left(\epsilon^2 \nabla c, \nabla \left(\Delta v\right)\right)$$

$$- \left\langle \epsilon^2 \Delta c, \nabla v \cdot \mathbf{n} \right\rangle + \left\langle \epsilon^2 g(c), \Delta v \right\rangle$$

$$:= B_d^{ch}(U, V).$$
(11)

The above equation has shown the following.

Proposition 3.1. Let $U \in H^4(\Omega)$ be a solution to the Cahn–Hilliard Eq. (3). Then,

$$U \in \mathcal{U}$$
 satisfies $B_d^{ch}(U, V) = 0, \quad \forall V \in \mathcal{V}.$ (12)

Remark 3.2. The methods employed in [31,34], which use a variational formulation different from Eq. (12), only considered periodic and trivial contact angle boundary conditions, with the latter one being imposed strongly on a rectangular mesh through algebraic constraints on the degrees of freedom. The last term in the third line of Eq. (11) enables the implementation of the general contact angle boundary conditions shown in Eq. (3c) on general geometries with non-conformal grids. As a consequence, the regularity requirement of the test functions in Eq. (12) is higher than that in [31,34].

Next, we show that the solution of the variational formulation Eq. (12) also satisfies Eq. (3), which includes the general contact angle boundary condition, Eq. (3c).

Proposition 3.3. Assume $U \in H^4(\Omega)$ satisfies the initial condition, Eq. (3d), and U solves the variational Eq. (12). Then U satisfies Eq. (3).

We need an intermediate result before we can prove Proposition 3.3.

Lemma 3.4 (Fourier's Lemma [51]). Let $m \in L^2(\Omega)$, such that,

$$(m, v) = 0, \quad \forall v \in \mathcal{D}(\Omega), \tag{13}$$

where $\mathcal{D}(\Omega)$ is the set of $C^{\infty}(\Omega)$ functions with compact support in Ω , then m=0 in Ω .

Proof. Because $\mathcal{D}(\Omega)$ is dense in $L^2(\Omega)$, there exists a Cauchy sequence $v_n \in \mathcal{D}(\Omega)$, such that $v_n \to \overline{m}$ in $L^2(\Omega)$, where $\overline{m} \in L^2(\Omega)$ is the complex conjugate of m. Then, we have

$$(m, v_n) \to (m, \overline{m}) = \int_{\Omega} |m|^2 = 0, \tag{14}$$

which implies m = 0. \square

Now, we are ready to show the proof of Proposition 3.3.

Proof of Proposition 3.3. Using integration by parts and moving all derivatives to the trial function, we can rewrite the variational formulation Eq. (11) into the following,

$$B_d^{ch}(U, V) = (\alpha, v) + \langle \beta_1, v \rangle + \langle \beta_2, \Delta v \rangle = 0, \quad \forall V \in \mathcal{V}, \tag{15}$$

where

$$\alpha = \frac{\partial c}{\partial t} - \Delta \left(f'(c) - \epsilon^2 \Delta c \right),\tag{16a}$$

$$\beta_1 = \nabla \left(f'(c) - \epsilon^2 \Delta c \right) \cdot \boldsymbol{n},\tag{16b}$$

$$\beta_2 = \epsilon^2 \left(\nabla c \cdot \mathbf{n} - g(c) \right), \tag{16c}$$

then, it is sufficient to show that Eq. (15) implies $\alpha = 0$ in Ω , and $\beta_1 = \beta_2 = 0$ on Γ . Recall that for any $v \in \mathcal{D}(\Omega)$ and any integer $j \geq 0$, the jth derivative of v vanishes on Γ , i.e., $D^j v|_{\Gamma} = 0$. Now taking $V \in \mathcal{D}(\Omega) \subset \mathcal{V}$, we have

$$0 = B_d^{ch}(U, V) = (\alpha, v). \tag{17}$$

Thus, Lemma 3.4 implies $\alpha = 0$. Next, we choose $v \in \mathcal{V}$ such that $v|_{\Gamma} = 1$ but $\Delta v|_{\Gamma} = 0$, and arrive at

$$0 = B_{\perp}^{ch}(U, V) = \langle \beta_1, v \rangle, \tag{18}$$

which implies $\beta_1|_{\Gamma} = 0$. Finally, we can show $\beta_2|_{\Gamma} = 0$ using a similar argument. \square

3.1.2. Split method

The high-order derivatives in the variational formulation of the proposed method Eq. (11), can be troublesome for the traditional finite element method which normally uses C^0 -continuous basis functions. Thus, an alternative approach is to split Eq. (3) into a system of two second-order PDEs by introducing an auxiliary unknown,

$$\mu = f'(c) - \epsilon^2 \Delta c \,. \tag{19}$$

Consequently, the trial and test functions become $U = \{c, \mu\} \in \mathcal{U}$ and $V = \{v, q\} \in \mathcal{V}$, respectively, with $\mathcal{U} = H^2(\Omega) \times H^2(\Omega)$ and $\mathcal{V} = H^1(\Omega) \times H^1(\Omega)$. Then Eq. (3) can be recast into the following variational formulation: find $U \in \mathcal{U}$, such that,

$$B_s^{ch}(U, V) := \left(\frac{\partial c}{\partial t}, v\right) + (\nabla \mu, \nabla v) + (\mu, q)$$

$$-\left(f'(c), q\right) - \left(\epsilon^2 \nabla c, \nabla q\right) + \left\langle\epsilon^2 g(c), q\right\rangle = 0, \quad \forall V \in \mathcal{V}.$$
(20)

Compared with Eq. (11), the regularity requirement of the trial and test function spaces in Eq. (20) is reduced. However, the discretization of Eq. (20) is more computationally expensive than that of Eq. (11) because of the additional unknown, μ .

3.2. Variational formulation of the isothermal Navier-Stokes-Korteweg equations

Following a similar strategy as in Section 3.1, we introduce the variational formulations of the isothermal Navier–Stokes–Korteweg equations using the proposed and the split methods.

3.2.1. Proposed method

We first introduce a space, $\widetilde{H}^2(\Omega) := H_0^1(\Omega) \cap H^2(\Omega)$, and let $U = \{\rho, \boldsymbol{u}\} \in \mathcal{U}$ and $V = \{\omega, \boldsymbol{v}\} \in \mathcal{V}$, for $\mathcal{U} = H^2(\Omega) \times [\widetilde{H}^2(\Omega)]^d$, and $\mathcal{V} = H^1(\Omega) \times [\widetilde{H}^2(\Omega)]^d$. If $U \in \mathcal{U}$ solves the isothermal Navier–Stokes–Korteweg Eq. (6), then U satisfies the following, $\forall V \in \mathcal{V}$,

$$B_{d}^{nsk}(U, V) := \left(\frac{\partial \rho}{\partial t}, \omega\right) - (\rho \boldsymbol{u}, \nabla \omega) + \left(\frac{\partial (\rho \boldsymbol{u})}{\partial t}, \boldsymbol{v}\right) - (\rho \boldsymbol{u} \otimes \boldsymbol{u}, \nabla \boldsymbol{v})$$

$$- (p(\rho), \nabla \cdot \boldsymbol{v}) + \left(\frac{1}{R_{e}} \boldsymbol{\tau}, \nabla \boldsymbol{v}\right) - \left(W_{e}^{2} \rho \nabla \rho, \nabla (\nabla \cdot \boldsymbol{v})\right)$$

$$- \left(\frac{1}{2} W_{e}^{2} |\nabla \rho|^{2}, \nabla \cdot \boldsymbol{v}\right) - \left(W_{e}^{2} \nabla \rho \otimes \nabla \rho, \nabla \boldsymbol{v}\right)$$

$$+ \langle W_{e}^{2} \rho s(\rho), \nabla \cdot \boldsymbol{v}\rangle = 0.$$
(21)

Note that the contact angle boundary condition, Eq. (6d), is imposed weakly in Eq. (21). Using a similar argument as in the proof of Proposition 3.3, we have the following.

Proposition 3.5. Assume $U \in H^2(\Omega) \times [\widetilde{H}^2(\Omega)]^d$ satisfies the initial data, Eqs. (6e) and (6f), and U solves Eq. (21). Then U satisfies Eq. (6).

3.2.2. Split method

Similar to the split of the Cahn-Hilliard equation, the isothermal Navier-Stokes-Korteweg equation can be rewritten into a system of second-order PDEs by introducing an additional unknown,

$$v = \Delta \rho. \tag{22}$$

The augmented trial and test functions are $U = \{\rho, \mathbf{u}, v\} \in \mathcal{U}$ and $V = \{\omega, \mathbf{v}, q\} \in \mathcal{V}$, for $\mathcal{U} = H^2(\Omega) \times [\widetilde{H}^2(\Omega)]^d \times H^1(\Omega)$ and $\mathcal{V} = H^1(\Omega) \times [H^1_0(\Omega)]^d \times H^1(\Omega)$. Then, Eq. (6) can be reformulated as: find $U \in \mathcal{U}$ such that, $\forall V \in \mathcal{V}$,

$$B_{s}^{nsk}(U, V) := \left(\frac{\partial \rho}{\partial t}, \omega\right) - (\rho \boldsymbol{u}, \nabla \omega) + \left(\frac{\partial (\rho \boldsymbol{u})}{\partial t}, \boldsymbol{v}\right) - (\rho \boldsymbol{u} \otimes \boldsymbol{u}, \nabla \boldsymbol{v})$$

$$- (p(\rho), \nabla \cdot \boldsymbol{v}) + \left(\frac{\boldsymbol{\tau}}{R_{e}}, \nabla \boldsymbol{v}\right) + \left(W_{e}^{2} \rho \boldsymbol{v}, \nabla \cdot \boldsymbol{v}\right) + \left(\frac{W_{e}^{2}}{2} |\nabla \rho|^{2}, \nabla \cdot \boldsymbol{v}\right)$$

$$- \left(W_{e}^{2} \nabla \rho \otimes \nabla \rho, \nabla \boldsymbol{v}\right) + (\boldsymbol{v}, q) + (\nabla \rho, \nabla q) - \langle s(\rho), q \rangle$$

$$= 0$$
(23)

Finally, we remark that the test function space of v, in the proposed method, Eq. (21), is $[\widetilde{H}^2(\Omega)]^d$, while that of the split method, Eq. (23), is $[H_0^1(\Omega)]^d$.

4. Space and time discretization

In this section, we discuss the space and time discretization used in this work. For simplicity, we use the Cahn–Hilliard equation with the proposed method, namely, Eq. (11), to demonstrate the spatial and temporal discretizations. The approximations of Eqs. (20), (21) and (23) follow a similar procedure, but they are not presented here for conciseness.

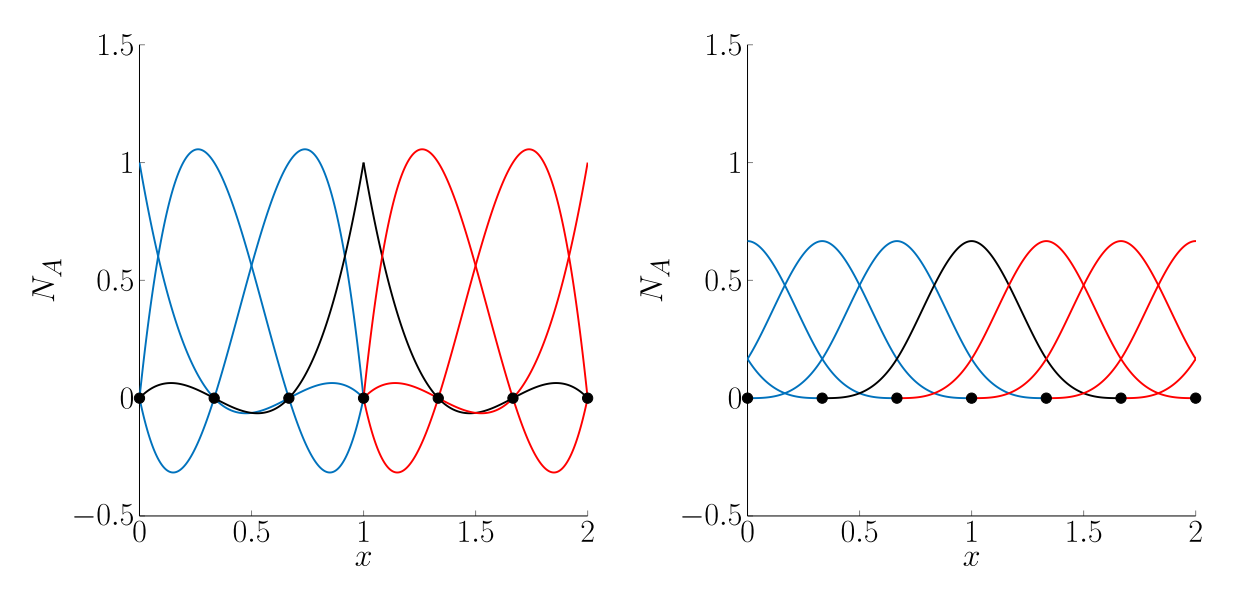


Fig. 1. Comparison of Lagrangian polynomials and B-spline basis functions. (Left) H^1 -conforming cubic Lagrangian polynomial basis functions with equally spaced nodes. (Right) H^3 -conforming cubic B-spline basis functions with equally spaced knots and C^2 inter-element continuity.

4.1. Spline basis

The proposed variational formulations, Eqs. (11) and (21), require H^3 - and H^2 -conforming test spaces respectively, which eliminates the use of traditional Lagrangian elements (H^1 -conforming) for spatial discretization. IGA uses spline basis functions which offer high-order continuity properties at the element boundary [30]. Splines of order p may be constructed with continuous derivatives of order (p-1). Fig. 1 shows a comparison between Lagrangian polynomials and C^2 -continuous B-splines of degree three. IGA with p=3 and p=2 or higher makes the discretization of Eqs. (11) and (21) possible, respectively. Following the works in [34,50], we construct the finite element space \mathcal{V}_h using IGA.

A generic spline basis function is denoted as N_A where the subscript "A" represents the control point index. In this paper, the weights of all the control points are set to be 1, thus NURBS reduce to B-splines in the usual tensor-product format; more discussion on IGA can be found in [30].

4.2. The semidiscrete formulation

We use the Galerkin method to approximate the variational formulation, Eq. (11). Let \mathcal{V}_h be a finite element subspace of \mathcal{V} , i.e.,

$$\mathscr{V}_h = \operatorname{span} \left\{ N_A \right\}_{A=1}^{n_b} \subset \mathscr{V}, \tag{24}$$

where n_b is the dimension of \mathcal{V}_h . An element $c_h \in \mathcal{V}_h$ can be expressed as

$$c_h = \sum_{A=1}^{n_b} c_A N_A, (25)$$

where c_A is the coefficient of the basis function N_A . Then, the approximation of Eq. (11) can be recast into the following: find $U_h = \{c_h\} \in \mathcal{V}_h$, such that,

$$B_d^{ch}(U_h, V_h) = 0, \quad \forall V_h \in \mathcal{V}_h. \tag{26}$$

4.3. Temporal discretization

The generalized- α method [52] is used for the temporal discretization. We define the residual vector as $\mathbf{R}^c = \{R_A^c\}_{A=1}^{n_b}$ such that

$$R_A^c := B_d^{ch} \left(U_h, N_A \right), \quad \text{for } N_A \in \mathcal{V}_h. \tag{27}$$

Let V and \dot{V} denote the vector of global degrees of freedom, $\{c_A\}_{A=1}^{n_b}$, and its time derivative respectively. The generalized- α algorithm can be stated as: given \dot{V}_n , V_n and $\Delta t_n = t_{n+1} - t_n$, find \dot{V}_{n+1} , V_{n+1} , $V_{n+\alpha_m}$ and $V_{n+\alpha_f}$ such that

$$\mathbf{R}^{c}\left(\dot{\mathbf{V}}_{n+\alpha_{m}}, \mathbf{V}_{n+\alpha_{f}}\right) = 0,\tag{28a}$$

$$V_{n+1} = V_n + \Delta t_n \dot{V}_n + \gamma \Delta t_n (\dot{V}_{n+1} - \dot{V}_n), \tag{28b}$$

$$\dot{V}_{n+\alpha_m} = \dot{V}_n + \alpha_m (\dot{V}_{n+1} - \dot{V}_n), \tag{28c}$$

$$V_{n+\alpha_f} = V_n + \alpha_f (V_{n+1} - V_n), \tag{28d}$$

where the subscript $(\cdot)_n$ denotes the respective value at the time instance t_n , Δt_n is the time-step size between t_{n+1} and t_n , and α_m , α_f and γ are real-valued parameters that are selected based on accuracy and stability. For a first-order linear ordinary differential equation system, second-order accuracy [53] is obtained if

$$\gamma = \frac{1}{2} + \alpha_m - \alpha_f,\tag{29}$$

while unconditional stability requires

$$\alpha_m \ge \alpha_f \ge \frac{1}{2}.\tag{30}$$

The parameters α_m and α_f can be further parametrized in terms of the spectral radius, $\rho_{\infty} \in [0, 1]$, as follows

$$\alpha_m = \frac{1}{2} \left(\frac{3 - \rho_\infty}{1 + \rho_\infty} \right), \quad \alpha_f = \frac{1}{1 + \rho_\infty}. \tag{31}$$

As a consequence, Eq. (30) is satisfied. We choose $\rho_{\infty} = 1/2$ for all the numerical simulations in this paper. The nonlinear system of equations is solved using Newton's method with both relative and absolute tolerances being 10^{-10} . The resulting linear system is solved using the preconditioned GMRES method [54]. Finally, the discrete systems are implemented using the PETSc package [55–58] and PetIGA [59].

5. Convergence results

In this section we perform convergence analyses of the proposed variational formulations and compare the convergence results with the split methods. For both the Cahn-Hilliard equation and the Navier-Stokes-Korteweg equations, a two-dimensional (d = 2) rectangular domain, $\Omega = (0, 5) \times (0, 1)$, is considered. The convergence analyses are performed using six uniform meshes with element size $h = 2^{-n}$, for n = 2, 3, ..., 7, in each direction. For each mesh, we solve Eqs. (11), (20), (21) and (23) using B-splines of degree p = 1, 2, ..., 5, which may vary depending on the variational formulations.

The equilibrium contact angle θ in Eqs. (4) and (10) is 60° for all simulations in this section. Because the contact angle is nontrivial ($\theta \neq 90^{\circ}$), neither analytical solutions or manufactured solutions [60] are available. Alternatively, the numerical solution obtained using the finest mesh ($h = 2^{-7}$) is considered as the reference solution. The convergence results for different meshes are obtained by comparing against the reference solution. A uniform time step $\Delta t = 0.001$ is used throughout the rest of the work, so that the temporal discretization errors are negligible compared to the spatial discretization errors.

5.1. Best approximation error of B-splines

The error analysis of higher-order nonlinear PDEs is rather difficult and is beyond the scope of this work. We instead present the best approximation error of B-splines [61–64].

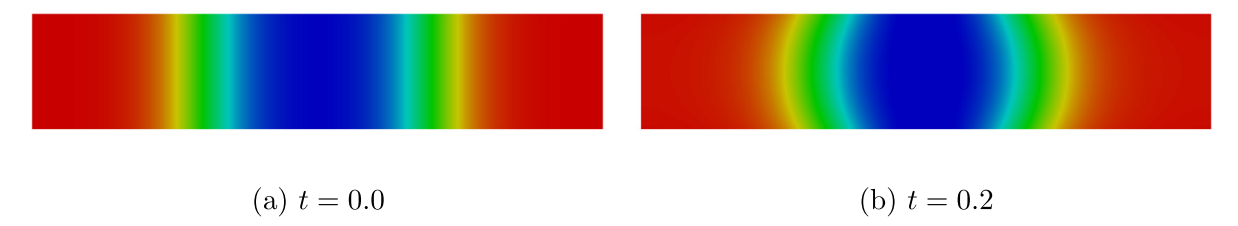


Fig. 2. The concentration field (c) at t = 0 and t = 0.2 of the Cahn-Hilliard Eq. (3). The results are obtained using the proposed method with p = 3, and $h = 2^{-6}$.

Theorem 5.1. For B-splines of order $p \ge 0$ and $0 \le r \le p+1$, the best approximation error of any $z \in H^{p+1}(\Omega)$ is given by

$$||z - z_h||_{H^r(\Omega)} \le Qh^{p+1-r}||z||_{H^{p+1}(\Omega)},\tag{32}$$

where Q > 0 is independent of h.

5.2. The Cahn-Hilliard equation

We choose $\epsilon = 0.3$ and $D_w = 0.05$ for the Cahn-Hilliard equation. The total simulation time is T = 0.2. At the initial time (t = 0), we place a slab of one of the components immersed in the other component; see Fig. 2(a). The slab is centered at $C_s = (2.5, 0.5)$ and has a width of 2. We regularize the interface using a hyperbolic tangent profile. The initial concentration is given by

$$c_0(\mathbf{x}) = \tanh\left(\frac{d(\mathbf{x}) - 1}{\sqrt{2}\epsilon}\right),\tag{33}$$

where d(x) is the Euclidean distance between x and C_s in the x direction, where x is the first component of x. The range of the concentration, c, is from -1.0 (blue) to 1.0 (red), where each extremum represents one component of the mixture. For the split method, the initial condition of the auxiliary parameter μ is obtained using Eqs. (19) and (33).

Fig. 2(a) shows the initial condition, Eq. (33), where the slab is attached to the wall with a 90° contact angle. The concentration at the final time is shown in Fig. 2(b) where the contact angle becomes 60° as we have imposed in Eq. (11) through the dynamic contact angle boundary condition given by Eqs. (4) and (3c).

The convergence results using the proposed (Eq. (11)) and the split (Eq. (20)) methods are presented in Fig. 3. For both formulations, (p + 1)-th order convergence rates of the concentration in the L^2 norm (see Fig. 3(a)) are obtained for B-splines of order p, and this agrees with the best approximation error presented in Theorem 5.1.

Fig. 3(b) shows the convergence results for the auxiliary parameter μ defined in Eq. (19) using the proposed and split methods. The L^2 norms of the error using the two approaches are very different. Such discrepancy is expected because the split method uses the same order (p) of approximation for both c and μ , while, for the proposed method, μ , which consists of the Laplacian of the concentration field, is obtained through postprocessing as shown in Eq. (19). However, the obtained convergence rates of μ in the L^2 norm, (p-1)-th order for the proposed method and (p+1)-th order for the split method, are in good agreement with the best approximation error.

Performing a detailed cost comparison of the two methods is challenging and out of the scope of this paper. We found, however, that using identical algebraic solver and basis functions, the average computational cost for the split method is 1.9 (serial) and 2.8 (parallel) larger than that of the proposed method in our implementation.

5.3. The isothermal Navier–Stokes–Korteweg equations

For the isothermal Navier–Stokes–Korteweg equations, the following model parameters are used: $\Theta = 0.85$, $W_e = 1/12$ and $R_e = 24$. The total simulation time is T = 50. The initial density field is plotted in Fig. 4(a) and can be expressed as

$$\rho_0(\mathbf{x}) = 0.35 + 0.25 \tanh\left(\frac{d(\mathbf{x}) - 1}{2W_e}\right),\tag{34}$$

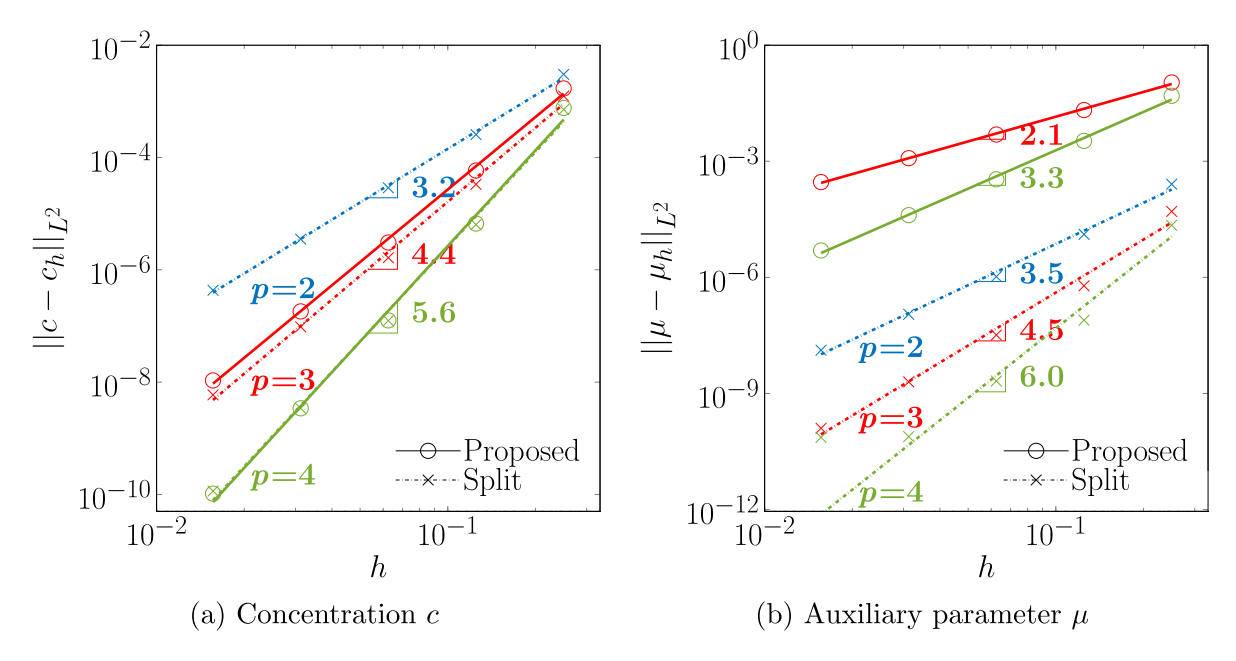


Fig. 3. Convergence results for the Cahn–Hilliard equation using the proposed (Eq. (11)) and split (Eq. (20)) methods with p = 2, 3, and 4. Notice for p = 2, only the results of the split method are shown, because the proposed method requires $p \ge 3$. For the proposed method, μ is calculated using Eq. (19). For the split method, μ is an additional variable.



Fig. 4. Density field (ρ) at t=0 and t=50 obtained from the Navier-Stokes-Korteweg Eqs. (6). The results are computed using the proposed method with p=3 and $h=2^{-6}$.

where d(x) is the same as in Section 5.2. In Eq. (34), the two extrema of ρ_0 , 0.1 (blue) and 0.6 (red), represent the Maxwell vapor and liquid density of water, respectively. We assume the initial velocity field is zero, i.e., $u_0(x) = 0$. For the split method, the initial condition of the auxiliary unknown ν can be obtained using Eqs. (22) and (34).

As shown in Fig. 4(a), the initial density profile given in Eq. (34) is close to the equilibrium state with a 90° contact angle. At the end of the simulation (t = 50), the equilibrium contact angle ($\theta = 60^{\circ}$) is observed in Fig. 4(b). Again, this verifies that the proposed method is effective in imposing the contact angle boundary condition.

The convergence results for the density ρ and velocity \boldsymbol{u} using the proposed and the split methods are presented in Fig. 5. For both methods, (p+1)-th order convergence rates are obtained for pth order B-splines. Therefore, we have recovered the optimal convergence rates as presented in Theorem 5.1.

Fig. 6 shows the convergence results of the auxiliary variable ν . For the proposed method, ν is calculated by taking the Laplacian of the density. We observe (p-1)-th order convergence rates for p=2,3, and 4. For the split method, ν is a primary variable. B-splines of the same order (p) are used for the density ρ , the auxiliary parameter ν , and the velocity ν . Even though, as presented in Fig. 5, the optimal convergence rates are observed for ρ and ν , Fig. 6(b) indicates that the convergence rates of ν are different for even and odd ρ using the split method. When $\rho=2$ and 4 (the top figure in Fig. 6(b)), we obtain (p+1)-th order convergence rates which are expected as presented in Theorem 5.1. When $\rho=1,3$ and 5 (the bottom figure in Fig. 6(b)), the convergence properties of ν are difficult to characterize.

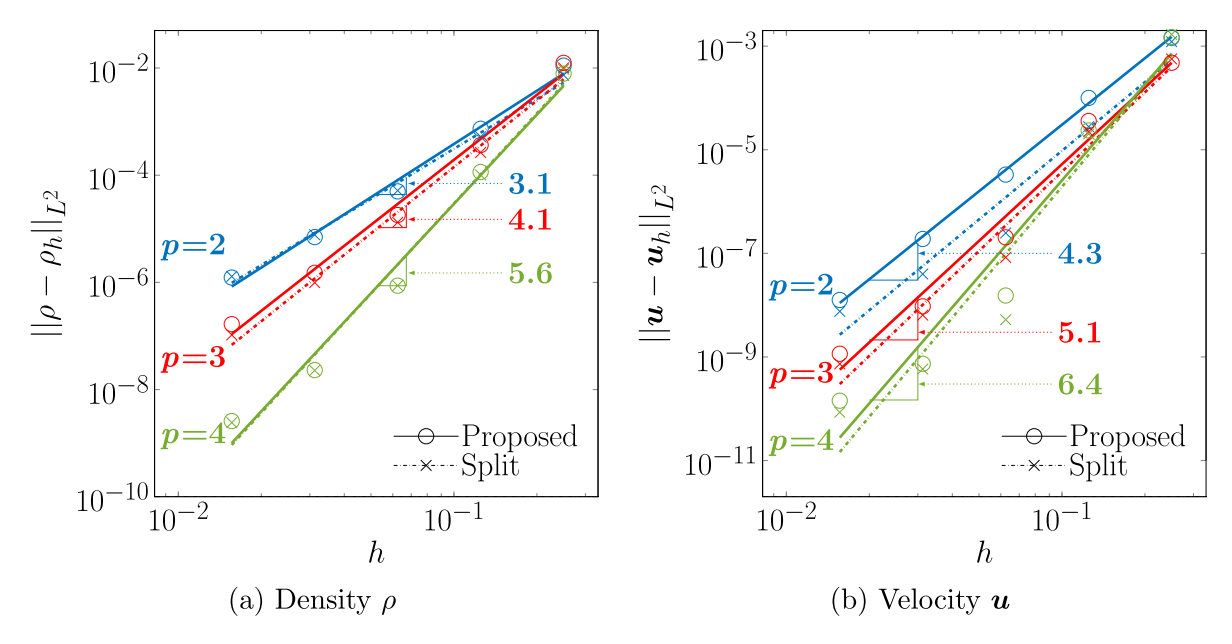


Fig. 5. Convergence results for the Navier–Stokes–Korteweg equations using the proposed (Eq. (21)) and split (Eq. (23)) methods with p = 2, 3, and 4. The convergence rates are shown to the right of the slope.

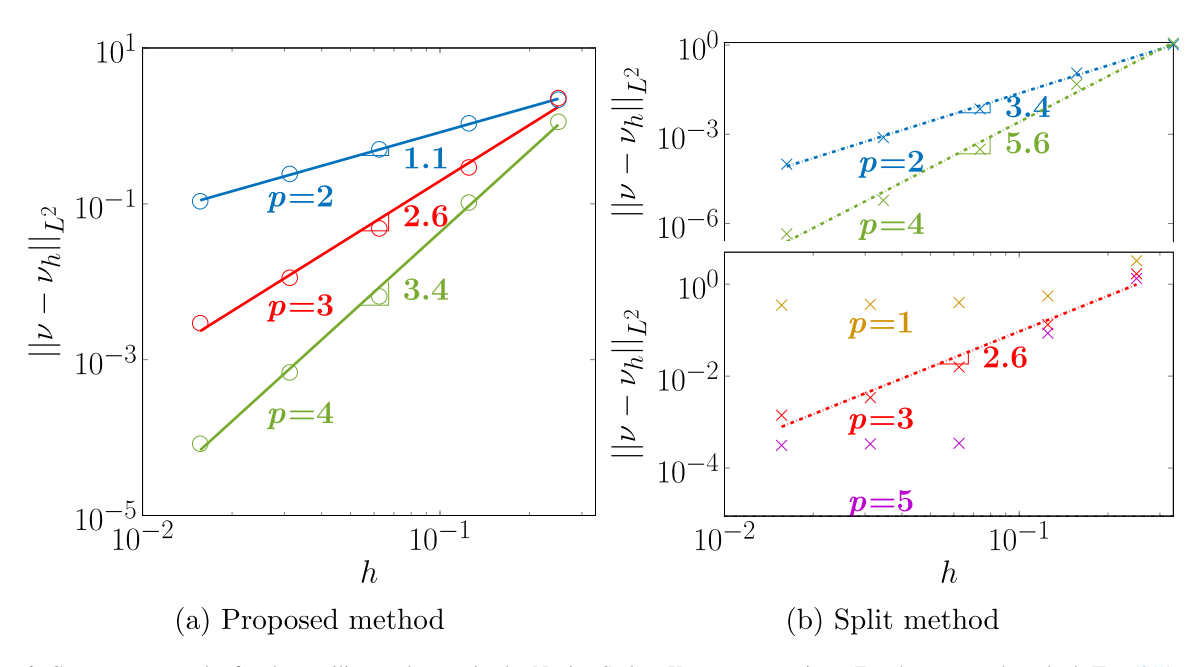
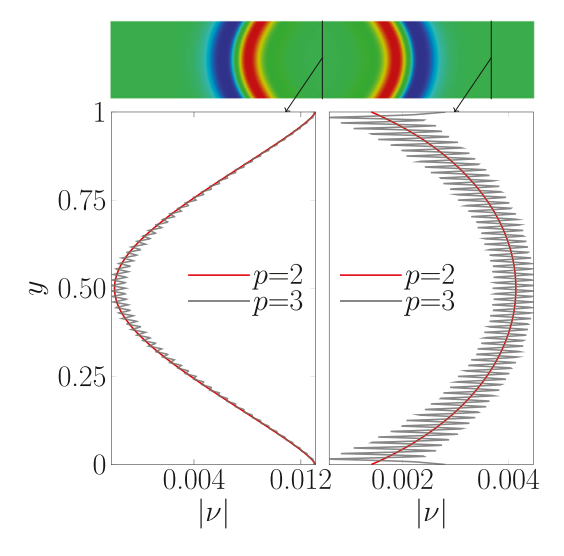


Fig. 6. Convergence results for the auxiliary unknown in the Navier–Stokes–Korteweg equations. For the proposed method (Eq. (21)), ν is calculated using Eq. (22). For the split method (Eq. (23)), ν is an additional variable.

The sub-optimal convergence properties of the auxiliary parameter ν using the split method and p=1,3, and 5 are due to oscillations as shown in Fig. 7 (Left). Oscillations occur for p=1,3, and 5 (results for p=1 and 5 are not shown) throughout the entire domain. For p=2 and 4 (results for p=4 are not shown), the auxiliary parameter is oscillation free. The origin of such oscillations using the split method deserves more thorough investigation but is beyond the scope of this work. In our implementation, using identical algebraic solver and basis functions, the split method is about 1.7 times slower than the proposed method, for both serial and parallel calculations.



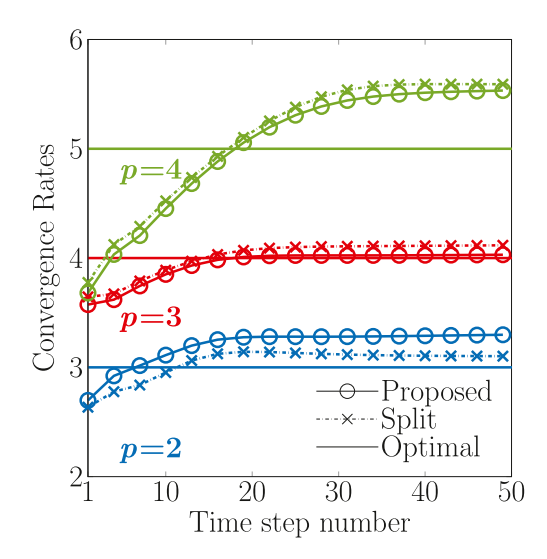


Fig. 7. (Left) The top plot shows the contour plot of ν over the whole domain for p=2. The bottom plots show the value of $|\nu|$ at x=2.5 (bottom left) and x=4.5 (bottom right) for p=2 and 3. All results shown are obtained at t=50. (Right) Time evolution of the convergence rates of the density ρ for the Navier–Stokes–Korteweg equations using p=2,3, and 4.

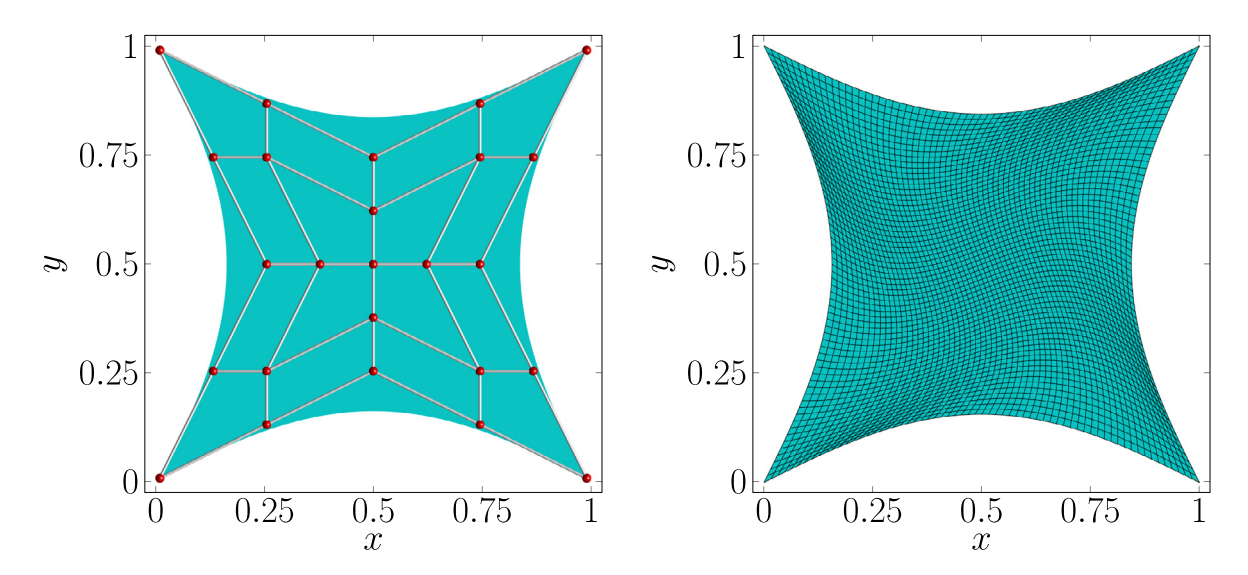


Fig. 8. Mesh generation for the Cahn-Hilliard equation. (Left) Initial control points η and the corresponding geometry with knots vector $\Xi_1 = \Xi_2 = [0, 0, 0, 0, 0, 1, 1, 1, 1, 1]$ and degree p = 4. The resulting basis functions are H^4 -conforming. (Right) Rotationally distorted ($\alpha_0 = 45^\circ$) and refined mesh consisting of 256 \times 256 elements. For every four knot lines, only one is plotted for the sake of clarity.

Finally, it is worth noting that the convergence rates reported in this section for the Navier–Stokes–Korteweg equations are obtained by allowing sufficient number of time steps for both methods (proposed and split). As shown in Fig. 7 (Right), the convergence rates of the density are sub-optimal at the beginning of the simulation. Optimal convergence rates are recovered only after sufficient number of time steps.

6. Numerical examples on mapped geometries

In this section, we use numerical examples for both problems to show that the proposed variational formulations (Eqs. (11) and (21)) are effective in imposing dynamic and static contact angle boundary conditions in more practical problems. To emphasize the generality of the proposed method, we adopt non-rectangular geometries with non-conformal grids. The domain of interest is a subset of $(0, 1) \times (0, 1)$ with non-rectangular shape. To generate the

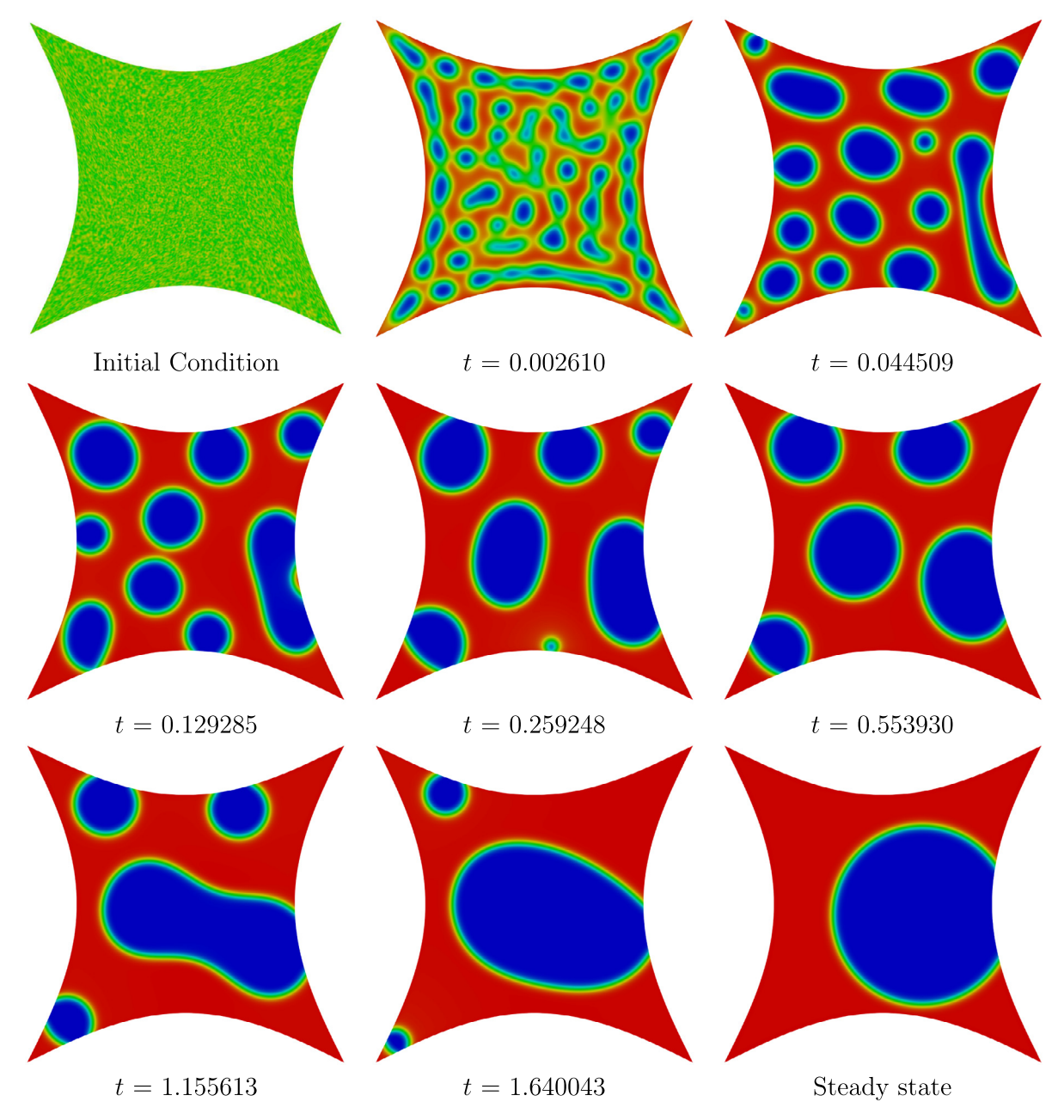


Fig. 9. Evolution of the concentration (c) for a randomly perturbed initial concentration profile with a mean value $\bar{c} = 0.2$.

desired meshes, we first give a set of control points η and knot vectors Ξ_1 , Ξ_2 , which determine the geometry and the global continuity of the basis functions. Then, we rotate the interior control points counter-clockwise by an angle α_0 with respect to the center of the domain, (0.5, 0.5). This step distorts the meshes without changing geometries. Finally, we insert non-repeating knots uniformly to refine meshes without reducing the continuity of the basis functions. The meshes used for the Cahn-Hilliard and Navier-Stokes-Korteweg equations are plotted in Figs. 8 and 10, respectively. Those two figures are visualized using NLIGA [65]. Unless otherwise specified, the model parameters of the Cahn-Hilliard equation and the isothermal Navier-Stokes-Korteweg equations are the same as in Sections 5.2 and 5.3, respectively. The contact angle, θ , is 45° in this section.

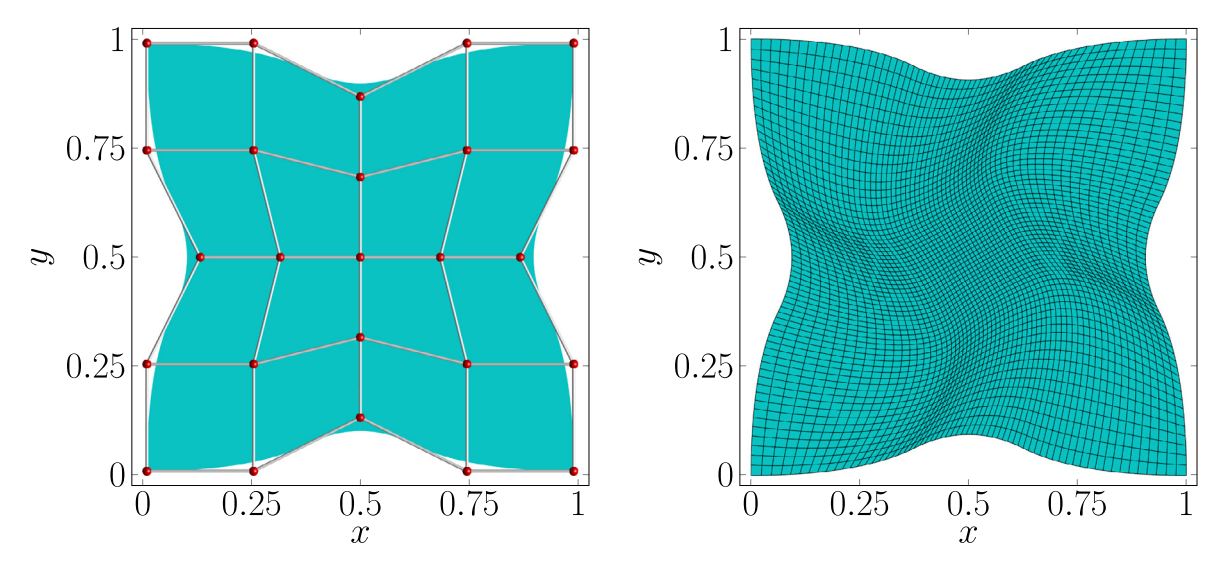


Fig. 10. Mesh generation for the isothermal Navier–Stokes–Korteweg equations. (Left) Initial control points η and the corresponding geometry with knots vector $\Xi_1 = \Xi_2 = [0, 0, 0, 1/3, 2/3, 1, 1, 1]$. The resulting basis functions are H^2 -conforming and have degree p = 2. (Right) Rotationally distorted ($\alpha_0 = 30^\circ$) and refined mesh consisting 256 \times 256 elements. For every four knot lines, only one is plotted for the sake of clarity.

6.1. The Cahn-Hilliard equation

For the Cahn-Hilliard equation, we simulate spinodal decomposition of a binary system. The length scale of the diffuse interface is $\epsilon=0.01$. The initial control points and the distorted mesh are shown in Fig. 8. For the initial condition, a stochastic concentration distribution $c_0=\bar{c}+r$ is considered with a mean value $\bar{c}=0.2$ and a random perturbation r.

Fig. 9 shows snapshots of the phase evolution. From its initial concentration distribution, the system separates into two phases whose composition is determined by the minima of the bulk free energy Eq. (5). During the evolution, the inclusions interact locally in order to minimize the gradient energy by reducing their number while increasing their characteristic lengths. The circular shape of a single inclusion is the outcome of this minimization procedure. It is also clear that the inclusions are attached to the wall with the specified contact angle, $\theta = 45^{\circ}$, both during the coarsening process and at steady state.

6.2. The isothermal Navier-Stokes-Korteweg equations

We simulate the evolution of five vapor bubbles immersed in a liquid pool for the isothermal Navier–Stokes–Korteweg equations. The initial control points and distorted mesh are shown in Fig. 10. The model parameters are given as follows: $W_e = 1/128$, $R_e = 256$ and $\Theta = 0.85$. At t = 0, there are five circular vapor bubbles in the domain. The centers of the bubbles are located at $C_1 = (0.41, 0.35)$, $C_2 = (0.125, 0.40)$, $C_3 = (0.40, 0.75)$, $C_4 = (1.00, 0.50)$ and $C_5 = (0.00, 0.00)$ respectively, with corresponding radii of $R_1 = 0.10$, $R_2 = 0.15$, $R_3 = 0.125$, $R_4 = 0.20$ and $R_5 = 0.20$. Then, the hyperbolic tangent density profile becomes,

$$\rho_0(\mathbf{x}) = -0.65 + 0.25 \sum_{i=1}^{5} \tanh\left(\frac{d_i(\mathbf{x}) - R_i}{2W_e}\right),\tag{35}$$

where $d_i(x)$ is the Euclidean distance between x and C_i , for i = 1, 2, ..., 5. Eq. (35) preserves the dimensionless density of the Maxwell equilibrium vapor ($\rho \approx 0.1$) and liquid ($\rho \approx 0.6$). In addition, the velocity is zero everywhere at the initial time.

Fig. 11 shows the time evolution of the density field. At the beginning of the simulation, the designated contact angle ($\theta = 45^{\circ}$) is quickly enforced for all vapor bubbles attached to the wall regardless of their initial contact

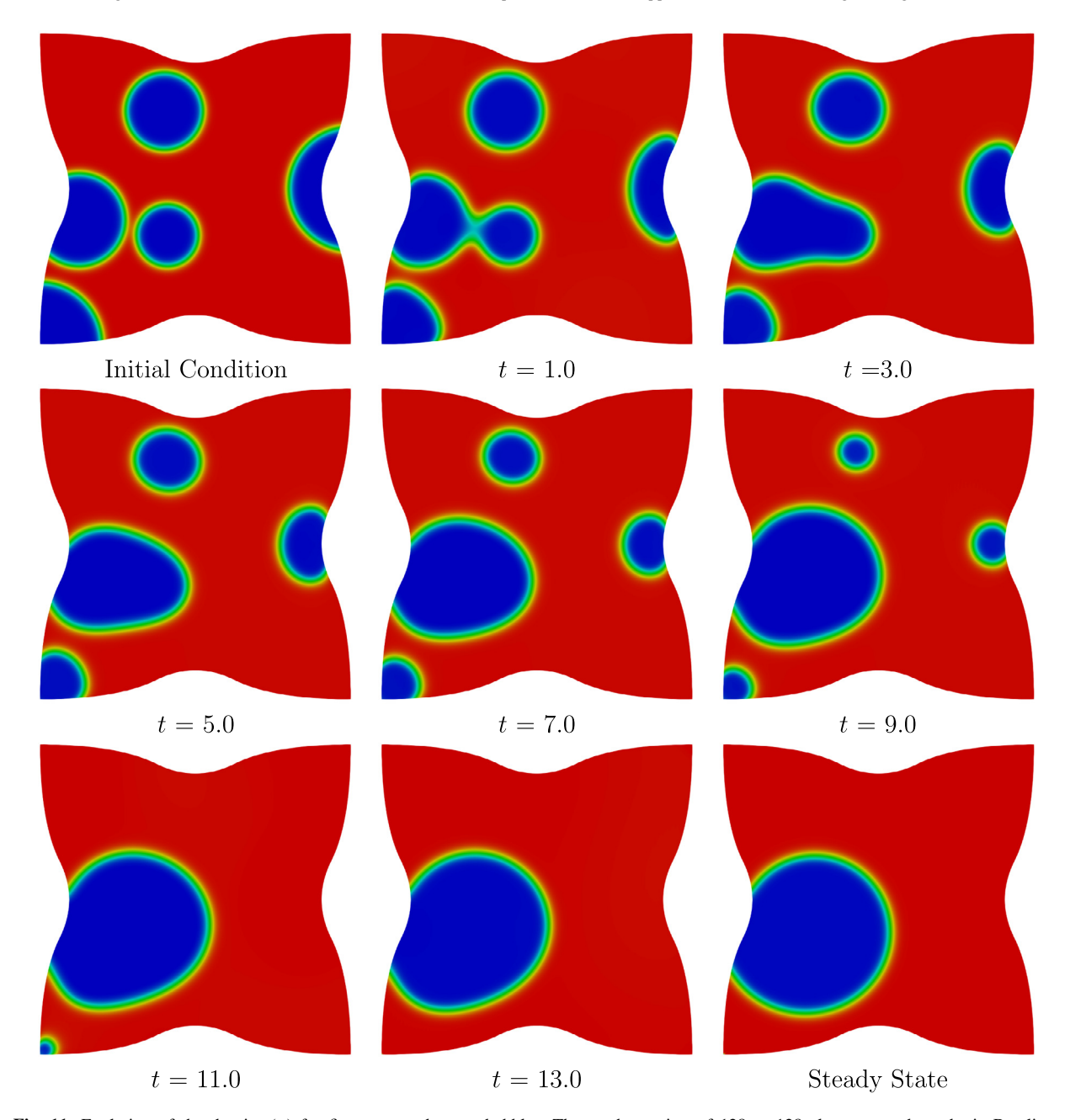


Fig. 11. Evolution of the density (ρ) for five separated vapor bubbles. The mesh consists of 128×128 elements, and quadratic B-splines are used (p=2).

angles at t = 0. The two bubbles located at the lower left corner gradually coalesce into a single large bubble, and evolve toward static equilibrium. The other three smaller bubbles eventually condense. This result is expected and can be explained as follows. The outer pressure that equilibrates a larger bubble is higher than the outer pressure that equilibrates a smaller bubble. Thus, smaller bubbles shrink and eventually condense in the system.

7. Conclusion

In this work, we have proposed a novel method to impose boundary conditions for higher-order PDEs. The Cahn-Hilliard equation and the isothermal Navier-Stokes-Norteweg equations are used as examples to demonstrate

the proposed method. Realistic (dynamic or static) contact angle boundary conditions can be imposed directly in the variational formulations, which have been shown to be equivalent to the original form of the PDEs if the solutions are smooth enough. Our proposed method avoids the addition of an auxiliary variable, which is inevitable in the classical split method. Our algorithm also avoids complications of other alternative approaches, such as the selection of a constant in Nitsche's method or the use of a stable pair of spaces in the method of Lagrange multipliers.

Although the proposed algorithm can be used with any weighted residual discretization that uses basis functions with high-order continuity, we illustrate it using IGA. Convergence analyses are conducted by comparing numerical solutions against a reference solution. Same order of convergence rates for the Cahn–Hilliard and isothermal Navier–Stokes–Korteweg equations are obtained for the proposed method and the split method using *h*-refinement. The convergence results agree with the best approximation errors of B-Spline basis functions. Finally, the effectiveness and generality of the proposed method in imposing static and dynamic contact angle boundary conditions is shown using numerical examples on mapped geometries and non-conformal grids.

There are many challenging problems not yet addressed in this work. It is necessary to show rigorous convergence analysis of the discrete problems. In addition, the auxiliary parameter of the Navier–Stokes–Korteweg equations using the split method exhibits oscillations if B-splines of odd order are used. The origin of such oscillations should be carefully studied.

Declaration of competing interest

The authors declare that they have no known competing financial interests or personal relationships that could have appeared to influence the work reported in this paper.

Acknowledgments

This work is funded partially by the U.S. Department of Defense (Award No. FA9550-20-1-0165) and partially by National Science Foundation, United States (Award No. 1805817).

References

- [1] S. Timoshenko, S. Woinowsky-Krieger, Theory of plates and shells, 1959.
- [2] R. Toupin, Elastic materials with couple-stresses, Arch. Ration. Mech. Anal. 11 (1) (1962) 385-414.
- [3] R.D. Mindlin, Microstructure in linear elasticity, Tech. rep., Columbia Univ New York Dept of Civil Engineering and Engineering Mechanics, 1963.
- [4] D. Burnett, The distribution of molecular velocities and the mean motion in a non-uniform gas, Proc. Lond. Math. Soc. s2-40 (1) (1936) 382-435.
- [5] S. Chapman, T.G. Cowling, The Mathematical Theory of Non-Uniform Gases: An Account of the Kinetic Theory of Viscosity, Thermal Conduction and Diffusion in Gases, Cambridge University Press, 1990.
- [6] H.E. Huppert, Flow and instability of a viscous current down a slope, Nature 300 (5891) (1982) 427-429.
- [7] D. Biskamp, E. Schwarz, J. Drake, Ion-controlled collisionless magnetic reconnection, Phys. Rev. Lett. 75 (21) (1995) 3850.
- [8] D. Biskamp, E. Schwarz, A. Zeiler, A. Celani, J. Drake, Electron magnetohydrodynamic turbulence, Phys. Plasmas 6 (3) (1999) 751–758.
- [9] V. Girault, P.-A. Raviart, Finite Element Approximation of the Navier-Stokes Equations, vol. 749, Springer Berlin, 1979.
- [10] F. Auricchio, L.B. da Veiga, A. Buffa, C. Lovadina, A. Reali, G. Sangalli, A fully "locking-free" isogeometric approach for plane linear elasticity problems: A stream function formulation, Comput. Methods Appl. Mech. Engrg. 197 (1–4) (2007) 160–172.
- [11] H. Emmerich, The Diffuse Interface Approach in Materials Science: Thermodynamic Concepts and Applications of Phase-Field Models, vol. 73, Springer Science & Business Media, 2003.
- [12] L.-Q. Chen, Phase-field models for microstructure evolution, Annu. Rev. Mater. Res. 32 (1) (2002) 113-140.
- [13] I. Steinbach, Phase-field models in materials science, Modelling Simulation Mater. Sci. Eng. 17 (7) (2009) 073001.
- [14] L. Ambrosio, V.M. Tortorelli, Approximation of functional depending on jumps by elliptic functional via t-convergence, Comm. Pure Appl. Math. 43 (8) (1990) 999–1036.
- [15] D. Nayigizente, S. Ducruix, T. Schmitt, Development of an interface thickening method for the direct numerical simulation of compressible liquid-vapor flows in the framework of the second gradient theory, Phys. Fluids 33 (5) (2021) 052119.
- [16] M. Shokrpour Roudbari, G. Şimşek, E.H. van Brummelen, K.G. van der Zee, Diffuse-interface two-phase flow models with different densities: A new quasi-incompressible form and a linear energy-stable method, Math. Models Methods Appl. Sci. 28 (04) (2018) 733–770.
- [17] M. Ambati, T. Gerasimov, L. De Lorenzis, A review on phase-field models of brittle fracture and a new fast hybrid formulation, Comput. Mech. 55 (2) (2015) 383–405.
- [18] Q. Du, C. Liu, X. Wang, A phase field approach in the numerical study of the elastic bending energy for vesicle membranes, J. Comput. Phys. 198 (2) (2004) 450–468.

- [19] A. Rätz, A. Voigt, et al., PDE's on surfaces—a diffuse interface approach, Commun. Math. Sci. 4 (3) (2006) 575–590.
- [20] D. Mokbel, H. Abels, S. Aland, A phase-field model for fluid-structure interaction, J. Comput. Phys. 372 (2018) 823-840.
- [21] W.J. Boettinger, J.A. Warren, C. Beckermann, A. Karma, Phase-field simulation of solidification, Annu. Rev. Mater. Res. 32 (1) (2002) 163–194
- [22] G. Lorenzo, T.J. Hughes, P. Dominguez-Frojan, A. Reali, H. Gomez, Computer simulations suggest that prostate enlargement due to benign prostatic hyperplasia mechanically impedes prostate cancer growth, Proc. Natl. Acad. Sci. 116 (4) (2019) 1152–1161.
- [23] C.M. Elliott, S. Larsson, Error estimates with smooth and nonsmooth data for a finite element method for the Cahn-Hilliard equation, Math. Comp. 58 (198) (1992) 603–630.
- [24] C.M. Elliott, D.A. French, F. Milner, A second order splitting method for the Cahn-Hilliard equation, Numer. Math. 54 (5) (1989) 575–590.
- [25] J. Barrett, J. Blowey, Finite element approximation of the Cahn-Hilliard equation with concentration dependent mobility, Math. Comp. 68 (226) (1999) 487–517.
- [26] J. Kim, K. Kang, J. Lowengrub, Conservative multigrid methods for Cahn-Hilliard fluids, J. Comput. Phys. 193 (2) (2004) 511-543.
- [27] L. Baňas, R. Nürnberg, A multigrid method for the Cahn-Hilliard equation with obstacle potential, Appl. Math. Comput. 213 (2) (2009) 290–303.
- [28] Y. Xia, Y. Xu, C.-W. Shu, Local discontinuous Galerkin methods for the Cahn-Hilliard type equations, J. Comput. Phys. 227 (1) (2007) 472–491.
- [29] K. Ammar, B. Appolaire, G. Cailletaud, F. Feyel, S. Forest, Finite element formulation of a phase field model based on the concept of generalized stresses, Comput. Mater. Sci. 45 (3) (2009) 800–805.
- [30] T.J. Hughes, J.A. Cottrell, Y. Bazilevs, Isogeometric analysis: CAD, finite elements, NURBS, exact geometry and mesh refinement, Comput. Methods Appl. Mech. Engrg. 194 (39–41) (2005) 4135–4195.
- [31] H. Gómez, V.M. Calo, Y. Bazilevs, T.J. Hughes, Isogeometric analysis of the Cahn-Hilliard phase-field model, Comput. Methods Appl. Mech. Engrg. 197 (49–50) (2008) 4333–4352.
- [32] S.A. Nazarov, G. Sweers, A hinged plate equation and iterated Dirichlet Laplace operator on domains with concave corners, J. Differential Equations 233 (1) (2007) 151–180.
- [33] P.K. Chan, A.D. Rey, A numerical method for the nonlinear Cahn-Hilliard equation with nonperiodic boundary conditions, Comput. Mater. Sci. 3 (3) (1995) 377–392.
- [34] M. Kästner, P. Metsch, R. De Borst, Isogeometric analysis of the Cahn-Hilliard equation—a convergence study, J. Comput. Phys. 305 (2016) 360–371.
- [35] R. Zhang, X. Qian, Triangulation-based isogeometric analysis of the Cahn-Hilliard phase-field model, Comput. Methods Appl. Mech. Engrg. 357 (2019) 112569.
- [36] D. Medina, N. Valizadeh, E. Samaniego, A.X. Jerves, T. Rabczuk, Isogeometric analysis of insoluble surfactant spreading on a thin film, Comput. Methods Appl. Mech. Engrg. 370 (2020) 113272.
- [37] A. Embar, J. Dolbow, I. Harari, Imposing Dirichlet boundary conditions with Nitsche's method and spline-based finite elements, Internat. J. Numer. Methods Engrg. 83 (7) (2010) 877–898.
- [38] S. Fernández-Méndez, A. Huerta, Imposing essential boundary conditions in mesh-free methods, Comput. Methods Appl. Mech. Engrg. 193 (12–14) (2004) 1257–1275.
- [39] J. Bueno, C. Bona-Casas, Y. Bazilevs, H. Gomez, Interaction of complex fluids and solids: theory, algorithms and application to phase-change-driven implosion, Comput. Mech. 55 (6) (2015) 1105–1118.
- [40] J. Bueno, Y. Bazilevs, R. Juanes, H. Gomez, Wettability control of droplet durotaxis, Soft Matter 14 (8) (2018) 1417-1426.
- [41] J.W. Cahn, J.E. Hilliard, Free energy of a nonuniform system. I. Interfacial free energy, J. Chem. Phys. 28 (2) (1958) 258-267.
- [42] J.W. Cahn, Phase separation by spinodal decomposition in isotropic systems, J. Chem. Phys. 42 (1) (1965) 93-99.
- [43] A. Carlson, M. Do-Quang, G. Amberg, Modeling of dynamic wetting far from equilibrium, Phys. Fluids 21 (12) (2009) 121701.
- [44] D. Jacqmin, Contact-line dynamics of a diffuse fluid interface, J. Fluid Mech. 402 (2000) 57-88.
- [45] S. Dong, On imposing dynamic contact-angle boundary conditions for wall-bounded liquid—gas flows, Comput. Methods Appl. Mech. Engrg. 247 (2012) 179–200.
- [46] H.G. Lee, J. Kim, Accurate contact angle boundary conditions for the Cahn–Hilliard equations, Comput. & Fluids 44 (1) (2011) 178–186.
- [47] D. Diehl, Higher Order Schemes for Simulation of Compressible Liquid-Vapor Flows with Phase Change (Ph.D. thesis), Verlag nicht ermittelbar, 2007.
- [48] J. Liu, C.M. Landis, H. Gomez, T.J. Hughes, Liquid-vapor phase transition: Thermomechanical theory, entropy stable numerical formulation, and boiling simulations, Comput. Methods Appl. Mech. Engrg. 297 (2015) 476–553.
- [49] S. Mukherjee, H. Gomez, Understanding how non-condensable gases modify cavitation mass transfer through the van der Waals theory of capillarity, Appl. Phys. Lett. 117 (20) (2020) 204102.
- [50] H. Gomez, T.J. Hughes, X. Nogueira, V.M. Calo, Isogeometric analysis of the isothermal Navier–Stokes–Korteweg equations, Comput. Methods Appl. Mech. Engrg. 199 (25–28) (2010) 1828–1840.
- [51] J.T. Oden, L. Demkowicz, Applied Functional Analysis, CRC Press, 2017.
- [52] J. Chung, G.M. Hulbert, A time integration algorithm for structural dynamics with improved numerical dissipation: The generalized-α method, J. Appl. Mech. 60 (2) (1993) 371–375.
- [53] K.E. Jansen, C.H. Whiting, G.M. Hulbert, A generalized-α method for integrating the filtered Navier–Stokes equations with a stabilized finite element method, Comput. Methods Appl. Mech. Engrg. 190 (3–4) (2000) 305–319.
- [54] Y. Saad, M.H. Schultz, Gmres: A generalized minimal residual algorithm for solving nonsymmetric linear systems, SIAM J. Sci. Stat. Comput. 7 (3) (1986) 856–869.

- [55] S. Abhyankar, J. Brown, E.M. Constantinescu, D. Ghosh, B.F. Smith, H. Zhang, Petsc/TS: A modern scalable ODE/DAE solver library, 2018, arXiv preprint arXiv:1806.01437.
- [56] S. Balay, S. Abhyankar, M.F. Adams, J. Brown, P. Brune, K. Buschelman, L. Dalcin, A. Dener, V. Eijkhout, W.D. Gropp, D. Karpeyev, D. Kaushik, M.G. Knepley, D.A. May, L.C. McInnes, R.T. Mills, T. Munson, K. Rupp, P. Sanan, B.F. Smith, S. Zampini, H. Zhang, H. Zhang, PETSc web page, 2019, URL https://www.mcs.anl.gov/petsc.
- [57] S. Balay, S. Abhyankar, M.F. Adams, J. Brown, P. Brune, K. Buschelman, L. Dalcin, A. Dener, V. Eijkhout, W.D. Gropp, D. Karpeyev, D. Kaushik, M.G. Knepley, D.A. May, L.C. McInnes, R.T. Mills, T. Munson, K. Rupp, P. Sanan, B.F. Smith, S. Zampini, H. Zhang, H. Zhang, PETSc Users Manual, Tech. Rep. ANL-95/11 Revision 3.14, Argonne National Laboratory, 2020, URL https://www.mcs.anl.gov/petsc.
- [58] S. Balay, W.D. Gropp, L.C. McInnes, B.F. Smith, Efficient management of parallelism in object oriented numerical software libraries, in: E. Arge, A.M. Bruaset, H.P. Langtangen (Eds.), Modern Software Tools in Scientific Computing, Birkhäuser Press, 1997, pp. 163–202.
- [59] L. Dalcin, N. Collier, P. Vignal, A. Côrtes, V.M. Calo, PetIGA: A Framework for high-performance isogeometric analysis, Comput. Methods Appl. Mech. Engrg. 308 (2016) 151–181.
- [60] L. Zhang, M.R. Tonks, D. Gaston, J.W. Peterson, D. Andrs, P.C. Millett, B.S. Biner, A quantitative comparison between C0 and C1 elements for solving the Cahn–Hilliard equation, J. Comput. Phys. 236 (2013) 74–80.
- [61] Y. Bazilevs, L. Beirao da Veiga, J.A. Cottrell, T.J. Hughes, G. Sangalli, Isogeometric analysis: approximation, stability and error estimates for h-refined meshes, Math. Models Methods Appl. Sci. 16 (07) (2006) 1031–1090.
- [62] L. Schumaker, Spline Functions: Basic Theory, Cambridge University Press, 2007.
- [63] R.A. DeVore, G.G. Lorentz, Constructive Approximation, vol. 303, Springer Science & Business Media, 1993.
- [64] S. Takacs, T. Takacs, Approximation error estimates and inverse inequalities for B-splines of maximum smoothness, Math. Models Methods Appl. Sci. 26 (07) (2016) 1411–1445.
- [65] X. Du, G. Zhao, W. Wang, M. Guo, R. Zhang, J. Yang, NLIGA: A MATLAB framework for nonlinear isogeometric analysis, Comput. Aided Geom. Design 80 (2020) 101869.